Silicon nitride based devices: lithographic mask roughness mitigation

Paulo Lourenço[*b,c], Alessandro Fantoni[a,c], João Costa[a,c], Manuela Vieira[a,b,c]

[a]ISEL/ADEETC - Instituto Superior de Engenharia de Lisboa, Instituto Politécnico de Lisboa, Área Departamental de Engenharia Eletrónica e Telecomunicações e de Computadores, Rua Conselheiro Emídio Navarro, 1, 1959-007 Lisboa, Portugal; [b]Faculdade de Ciências e Tecnologia, FCT, Universidade Nova de Lisboa, Departamento de Engenharia Eletrotécnica, Campus da Caparica, 2829-516 Caparica, Portugal; [c]CTS-UNINOVA, Campus da Caparica, 2829-516 Caparica, Portugal

ABSTRACT

Lithographic technology has been one of the main upholders to Moore's law in the semiconductor industry for the last decades. The underlying reason that enabled the evolution in semiconductor industry has been a steady silicon wafer printing cost, while being able to dramatically increase the number of nodes that can be printed per chip. Key developments in lithography such as wavelength decreasing, together with performance increase in lens and imaging technology, should be accounted for almost all the reduction of cost per function in integrated circuits technology.

In this work, we will be presenting the simulation of two mitigation techniques for the impact of defects introduced by manufacturing processes. Namely, the lithographic mask limited resolution on the geometry of the representative device. These perturbations are a consequence of the lithographic mask limited resolution on the geometry of the representative device. For this purpose, the Beam Propagation and Finite Differences Time Domain methods will be used to simulate a multimode interference structure based on silicon nitride. The structure will be affected by previously mentioned perturbations and we expect results revealing a strong dependence between mask resolution, and imbalance and power loss.

Two strategies will be followed concerning the mitigation of power loss and imbalance introduced by the limited resolution of lithographic mask:

- Access waveguides tapering;

- Adjustable power splitting ratios through the electro-optic effect.

Through both strategies we aim to achieve an improvement on device's performance but, in the latter are expected finer tuning capabilities, being enabled by dynamic compensation of power loss and imbalance when in a closed loop control architecture.

Keywords: Beam Propagation Method, Finite Differences Time Domain, Multimode Interference, 3 dB splitter, lithographic mask resolution, graphene, chemical potential

1. INTRODUCTION

The remarkable success of lithographic technology in semiconductor industry, has persuaded the transference and adaptation of this technology to device manufacturing in the Photonic Integrated Circuit (PIC) industry. However, optical devices present a much higher sensitivity to lithographic imperfections, when compared to the electronic counterparts.

[*] pj.lourenco@campus.fct.unl.pt

This greater reactiveness to imperfections is explained, mainly, by the wavelength at which such devices operate, being similar to the wavelength used for mask transfer [1],

$$Resolution = k_1 \frac{\lambda}{NA} \quad (1)$$

where, k_1 is a constant that depends on the used process (for integrated circuits manufacturing, $k_1 = 0.5\ to\ 0.8$) and NA is the numerical aperture of the optical lithographic tool (usually $NA = 0.5\ to\ 0.6$).

Only a selected few manufacturers have access to state-of-the-art foundries, where resolutions of 100 nm or less are a reality. In most facilities that are able to fabricate such structures, namely research institutes and universities, lithographic mask defects present a performance constraint that must be better understood and mitigated.

On the other hand, hydrogenated amorphous silicon has been extensively used in many real life applications, from thin film transistors in advanced displays to photodetectors [2], [3]. This material has also been considered a reliable platform candidate for the fabrication of PICs. There has been reports in the literature from interconnect waveguides to functional devices, based in this technology [4].

The interest in using this material is mainly explained by its deposition being possible at low temperatures through Plasma Enhanced Vapour Deposition (PECVD), which makes it back-end compatible with Complementary Metal Oxide Semiconductor (CMOS) manufacturing processes [5]. Moreover, when deposited over silicon dioxide, the created structures present high refractive index contrast, which permits the development of submicron cross section waveguides, with the possibility of describing very small radius bends and, consequently, leading to very high circuit density integration. However, the spectral absorption of hydrogenated amorphous silicon is located within the visible range, being transparent at wavelengths longer than 1 micro-meter [6].

This work is part of a wider project, consisting on the development of a biomedical plasmonic sensor. The device functionality is based on the coupling of propagating modes in a dielectric waveguide and the surface plasmon resonance generated on the overlaid metallic layer. This sensor operating wavelength must be located within the visible part of the spectrum, so the detection outcome readout might be accomplished by an a-Si:H based photodetector.

To fulfil the need for structure transparency in the visible range, silicon compounds may be synthesized. Such is the case of silicon nitride (Si_3N_4) that presents a substantially low extinction coefficient for electromagnetic (EM) energies within the range $380 - 780\ nm$ (violet to red).

Also, the present work materializes as a natural extension of previous research [7], [8] where perturbations, introduced along the edges of an MMI device by fabrication processes, are simulated and their influence in the overall performance of the structure is evaluated. Moreover, the latter work [8] reports a statistical analysis of the impact of lithographic mask defects, when considering the manufacturing of a batch of samples and where each sample is affected by an independent random distribution of defects.

2. METHODS

2.1 The MMI 3dB coupler

The simulated structure is depicted in Figure 1. It consists on an input waveguide, the middle section which is wide enough to support the MMI phenomenon and two output waveguides. The semiconductor used for the wave-guiding structure is Si_3N_4, for this material transparency is within the visible range ($\lambda = 0.65\ \mu m$). The height/width of both input and output waveguides were selected to assure single mode operation and the input field consisted on the Transverse Electric (TE – 3D) fundamental mode.

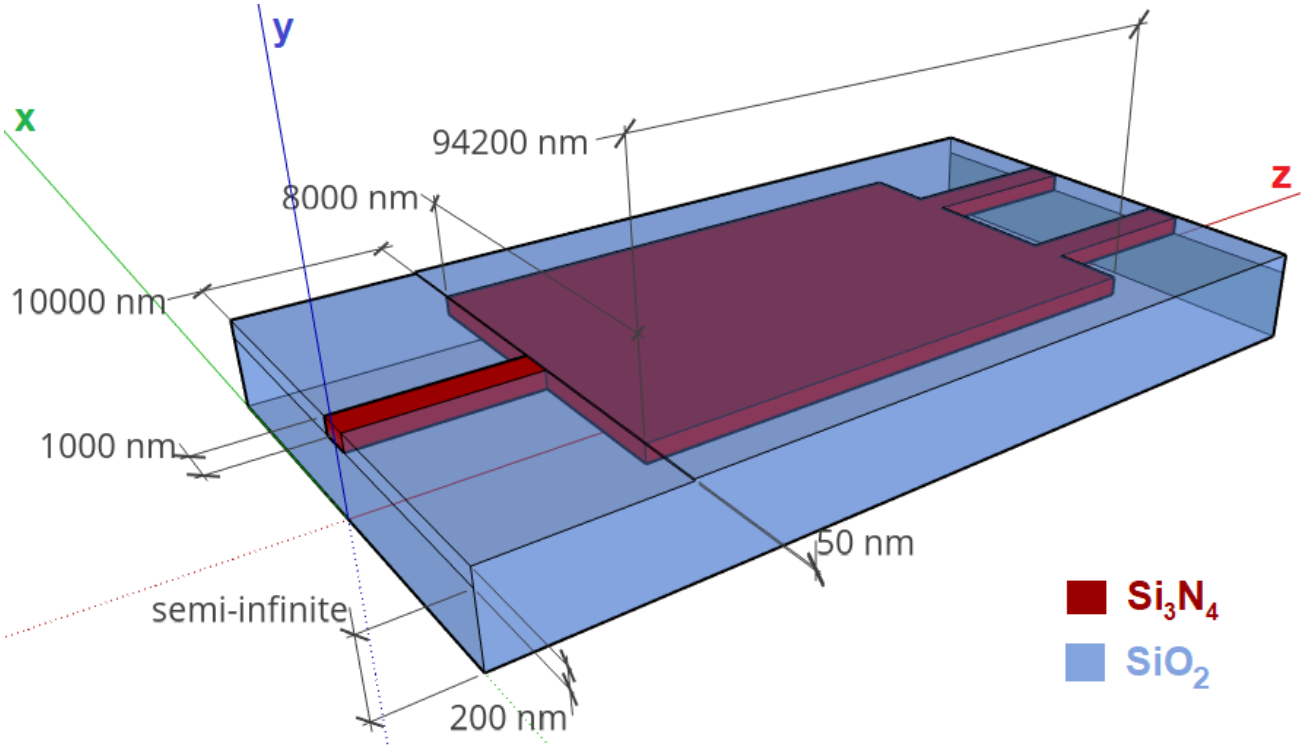

Figure 1 - Generic 1x2 MMI structure geometry and dimensions.

MMI devices rely on the self-imaging principle which states that single or multiple images of a given input field profile are replicated periodically in space as the electromagnetic field propagates through the waveguide [9], [10]. The propagation constant of a mode β_m (m = 0, 1, 2, ...), propagating in a high contrast step index multimode device, shows an approximate quadratic dependence to the mode number m:

$$\beta_m \cong k_0 n_{core} - \frac{(m+1)^2 \pi \lambda_0}{4 n_{eff} W_{eff}^2} \tag{2}$$

where k_0 is the vacuum wavenumber, n_{eff} the effective refractive index of the structure, λ_0 the vacuum wavelength, and W_{eff} the effective width of the MMI waveguide. The effective refractive index, n_{eff}, is a characteristic of each propagating mode, representing the "experienced" refractive index, when propagating inside the waveguide structure and the standing-wave condition is matched [10]. Hence, the n_{eff} of a given propagating mode may be calculated as in Equation (3) below:

$$n_{eff} = n_{core} \sin \theta_p \tag{3}$$

where n_{core} is the core media refractive index, and θ_p is the refraction angle of the transmitted field with respect to the normal at the input interface and at the point of reflection. The effective width, W_{eff}, is the width when considering the mode field profile penetration depth, due to the Goos-Hähnchen shifts, into the waveguide boundaries. This dimension is polarization dependent and in high refractive index contrast devices, the penetration depth of the EM field beyond the inner walls of the device is practically non-existent, hence W_{eff} can be approximated by the effective width of the fundamental mode [9]:

$$W_{eff} \cong W_{m0} \tag{4}$$

The spatial location of single/multiple and direct/mirrored images, resulting from the propagation modes interference, is directly related to the beat length (L_π) of the two lowest order modes:

$$L_\pi = \frac{\pi}{\beta_0 - \beta_1} \cong \frac{4n_{eff}W_{eff}^2}{3\lambda_0} \cong \frac{4n_{eff}W_{mo}^2}{3\lambda_0} \quad (5)$$

Single mirrored and direct images from the input field profile form at $3L_\pi$ and $2(3L_\pi)$, respectively, while two-fold images form at $1/2(3L_\pi)$ and $3/2(3L_\pi)$. Single images are, approximately, the same amplitude as the input EM field and each of the two-fold images is affected by a 3 dB attenuation factor, thus offering the ideal conditions for a power splitter device, similar to the structure diagram depicted in Figure 1. This schematic represents a Si_3N_4 MMI device embedded in SiO_2 and associated dimensions, which were used throughout this paper in our simulations and subsequent analysis.

Moreover, by using an interference mechanism designated as symmetric interference, 1 × N power splitters may be designed with quarter-length MMI sections. The mechanism relies on preventing the excitation of odd order modes within the multimode section of the structure. This is attained by placing the input waveguide, with a propagating symmetric field profile (e.g., Gaussian beam), at the width center of the MMI section, thus resulting in N linear combinations of the input profile located at:

$$L = \frac{p}{N}\left(\frac{3L_\pi}{a}\right) \quad (6)$$

where $p \geq 0$, $N \geq 1$, p, and N are integers, have no common divisor and p/N represents 1st, 2nd, …, n^{th} single and N-fold images at location L; a denotes the type of coupler (for a 1 × N power splitter, $a = 4$).

According to the literature [11], excess loss and imbalance between the output waveguides are two of the most influent characteristics on a 3 dB MMI coupler, when considering its performance. These constraints are due to deviations from the geometry of the ideal device, introduced by fabrication tolerances. Imbalance is particularly disadvantageous in our case. Being this research part of a broader project that intends to develop a biomedical plasmonic sensor and where there will be a reference and a sensing arms, power imbalance between the outputs will result in a reduction of sensing capabilities.

This work will take into consideration two approaches to mitigate the impact of the main causes of excess loss and power imbalance in these devices, namely the lithographic mask limited resolution:

- The insertion of tapers to adapt the width mismatch between the access waveguides and the wider MMI section;
- By using graphene sandwiched between dielectric waveguides and placed at strategic locations along the MMI structure to control the influence of propagating modes inside the multimode section.

2.2 Background

Graphene has been a subject of intense research for some years now, because of its remarkable electronic and optical properties. It presents flexibility, robustness, environmental stability [12] and singular optical properties, such as, strong light coupling [13] and optical conductivity controlled by bias gating [14]. This gate variable optical conductivity is of high interest for electro-optical (EO) modulation.

According to Lu et al. [15], there are two absorption processes in light-graphene interaction. These processes are the inter-band and intra-band absorptions, which together characterize the complex conductivity of graphene:

$$\sigma_t = \sigma_{intra}(\omega, \mu_c, \Gamma, T) + \sigma_{inter}(\omega, \mu_c, \Gamma, T) \quad (7)$$

where, ω is the light angular frequency, μ_c is the chemical potential, Γ is the charged particle scattering rate and T is the temperature. Because the chemical potential may be electrically controlled, the conductivity of graphene can be tuned through gating voltage V_f.

In this work, we evaluated the evolution of the permittivity of graphene with the chemical potential, at the wavelength of operation for our MMI structure ($0.65\ \mu m$), to determine if this feature of graphene could also be exploited at this wavelength. Figure 2 presents the behavior of graphene for our particular case:

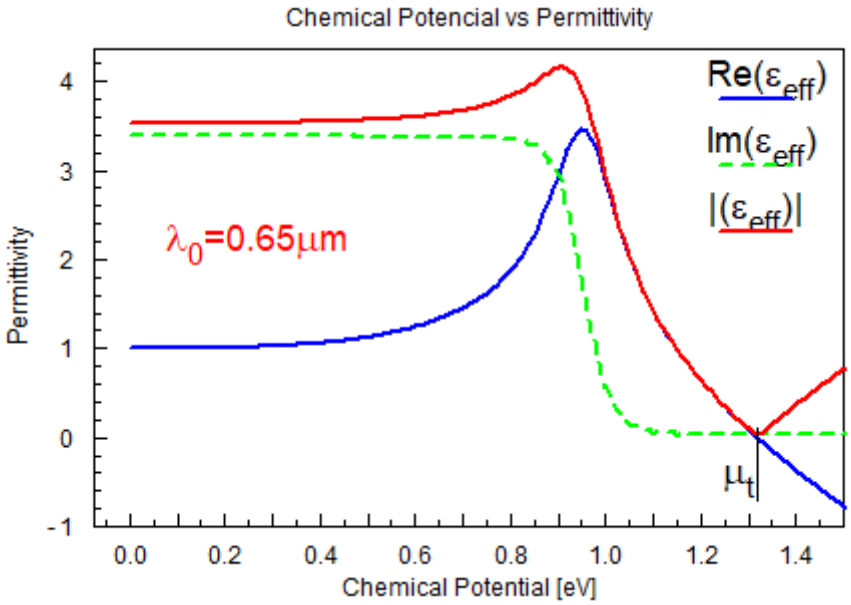

Figure 2 - Permittivity of graphene with the chemical potential at the 650 nm wavelength.

As can be observed in the above figure, at the operating wavelength of $0.65\ \mu m$, when the chemical potential reaches ~1.325 eV and further, the real part of graphene permittivity crosses zero while the imaginary part remains constant. This corresponds to a sign inversion of the real part of permittivity and is usually associated to a resonance often described as the "near-zero-epsilon". Such effect is not a particularity of graphene, for many other materials [16], [17] also possess a plasma frequency which is characterized by a metallic-like behavior, only in graphene this resonance may be reached through electrical gating.

3. SIMULATIONS

In previous work [7], [8], we assessed through numerical simulations the width offset from the ideal geometry of the MMI device, which is introduced by manufacturing processes. In this paper, we keep the same approach regarding the structure design conditions. The simulated structure consists of input and output waveguides, and the MMI section, affected by independent defects distributions along longitudinal edges.

Defects distribution standard deviation influences the width (x-axis) of all structure sections, along the propagation length (z-axis), and are independent in each section of the structure (input and output waveguides and MMI section). It was assured that defects on the left and right longitudinal edges of each section were not correlated to one another, nor even within sections. The correlation length of the random distributions of defects was selected as the full length of each section (access waveguides and multimode sections), to properly emulate real-world distribution of perturbations.

A silicon nitride waveguide buried in silicon dioxide is not a usual waveguide design. However, there are some reports in the literature which have implemented similar technology. Namely, for the manufacturing of such a device, the process could rely on a bottom thermal SiO_2 substrate, followed by Plasma Enhanced Chemical Vapor Deposition (PECVD) of the Si_3N_4 waveguide and an SiO_2 cladding, which can be obtained by a PECVD process [18] or by plasma gas decomposition [4].

3.1 Access waveguides taper

At this stage, our work considered the evaluation of the impact of inserting linear tapers in each access waveguide. Beam Propagation Method (BPM) [19] simulations were carried out on a device with the characteristics presented in Figure 3, where it is evident the impact of the random distribution of defects along the longitudinal edges of the structure.

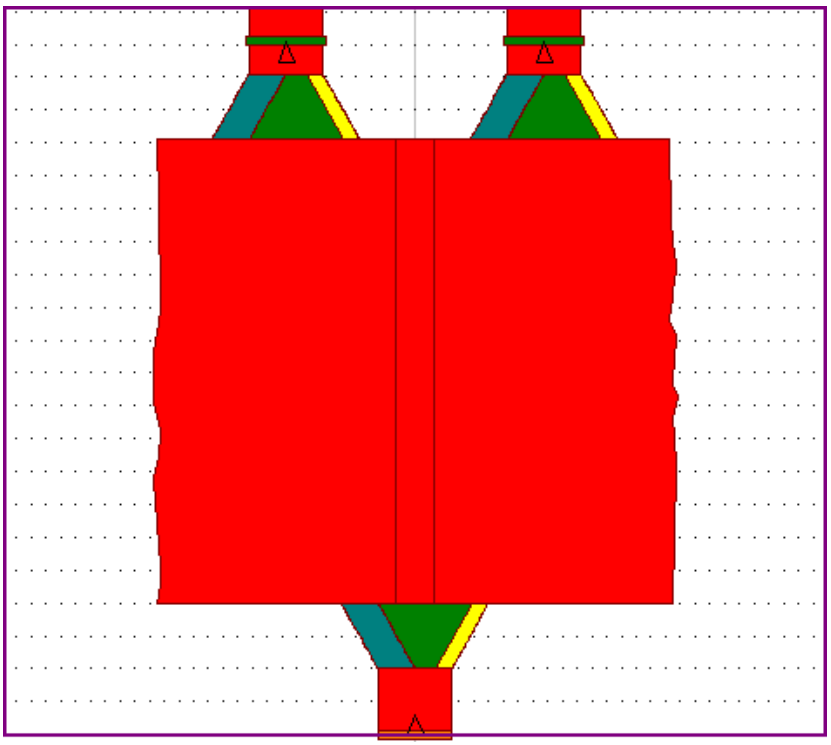

Figure 3 - Simulation workspace of the tapered MMI structure.

The simulated device had the following characteristics and the MMI section length was determined considering Equation (7), with corresponding parameters for a 3 dB power splitter device (p = 1, N = 2 and a = 4):

- 1 × 0.2 × 10 μm for input and output waveguides width, height and length, respectively;
- 8 × 0.2 × 90.4 μm for MMI section's width, height and length, respectively;
- The MMI device is completely embedded in SiO_2 with a 50 nm cover and the superstrate is air.

Next, we defined the power imbalance between the output waveguides as the ratio represented by Equation (8):

$$Imbalance = \frac{Out_2 - Out_1}{Out_2 + Out_1}. \quad (8)$$

Simulations were conducted considering the operating wavelength $\lambda = 0.65\ \mu m$, the TE fundamental mode as the input field and 10 nm standard deviation for the random distribution of defects, while iterating the width of the linear tapers located between the multimode section and the access waveguides. By monitoring the power at the end of the output waveguides, we were able to obtain the results presented in Figure 4:

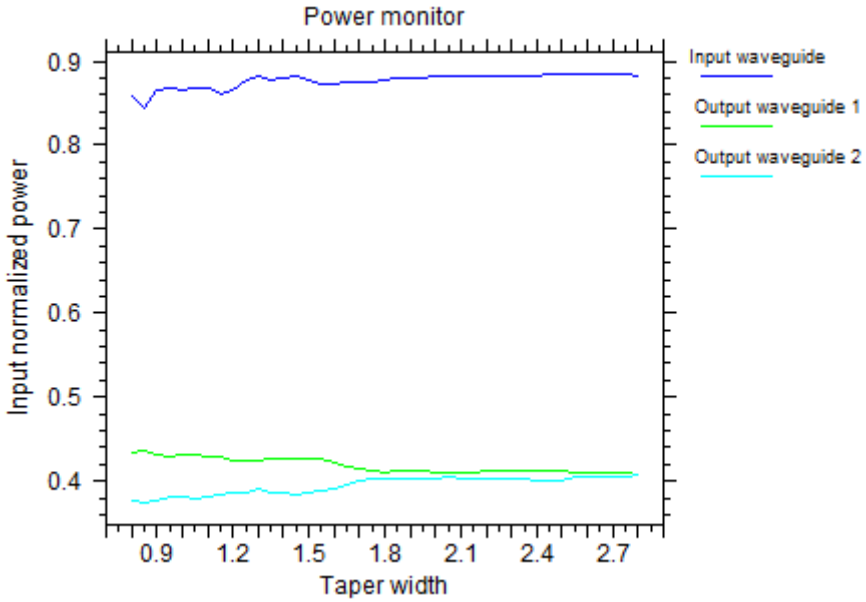

Figure 4 - Power imbalance and insertion loss vs taper width.

The above figure clearly shows that, as the taper width increases, the field intensity at both the output waveguides converges, hence minimizing power imbalance. As a consequence, the insertion loss also decreases which is denoted by a slight increase on the monitored input power. These results seem to be in accordance with the work presented in [11], which states that the optimal access waveguide width should be approximately 0.3 of the multimode section width.

3.2 Dynamic tuning

As stated before in this paper, optical conductivity of graphene may be controlled by bias gating. We propose that, by placing layers of graphene at strategic locations, namely where direct/mirrored images of the input profile are formed within the MMI section, we might be able to control independently the influence of a given image or images on the corresponding affected output. If this control bias depends on the output power verified in one of the exiting waveguides then, by negative/positive feedback, we might be able to dynamically tune the imbalance verified between output waveguides.

In Figure 5 is presented an MMI structure, where the propagating field is controlled by the bias applied on the graphene layer. By varying the chemical potential of graphene, one is able to affect its resonance at a given wavelength, hence the propagating field intensity may be modulated through bias gating of graphene.

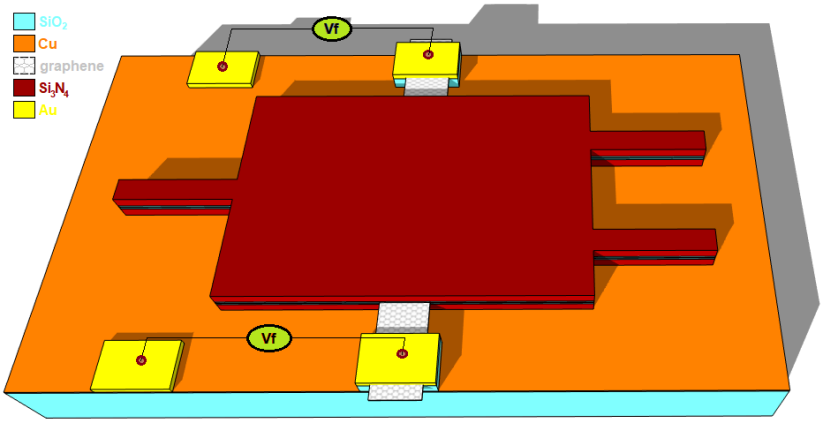

Figure 5 - Schematic of MMI structure with control through bias gating of graphene.

Based on Figure 2 and the results presented regarding the change on the dielectric constant with increasing chemical potential, we used a mode solver to determine the modal index of the TE fundamental mode on a multilayer waveguide 2 µm wide and with the following layers composition:

- Si_3N_4 height = 90 nm;
- SiO_2 height = 10 nm;
- Graphene height = 0.7 nm;
- SiO_2 height = 10 nm;
- Si_3N_4 height = 90 nm;

We also considered SiO_2 as the substrate and air for the cladding. Figure 6a) represents the transverse refractive index profile of the waveguide utilized by the mode solver to determine the TE fundamental mode supported by the multilayer waveguide. Figure 6b) shows the fundamental mode profiles when the chemical potential of graphene is 0 eV (top) and 1.325 eV (bottom). Please, note the difference between the imaginary parts of the modal indices present at the top and bottom profiles. The bottom profile presents a value almost two orders of magnitude lower!

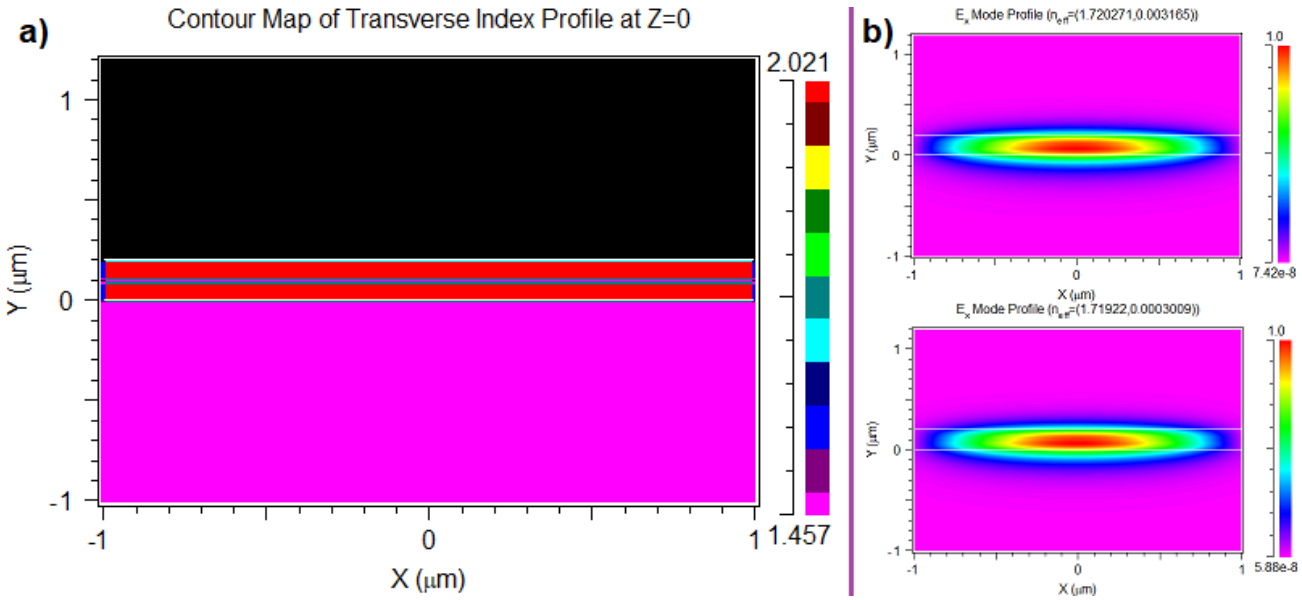

Figure 6 – a) Transverse refractive index profile of simulated waveguide; b) [top] – fundamental mode profile when U_C=0 eV; b) [bottom] – fundamental mode profile when U_C=1.325 eV.

The complex value of the propagation constant of a given mode is defined as in Equation (9):

$$n_c = n + ik \tag{9}$$

where, n and k correspond to the real and the imaginary parts, respectively, of complex value n_c; k is often referred to as the extinction coefficient and is directly related to the absorption of the material. On the other hand, the correspondence between the refractive index and permittivity of a material is given by Equations (10) and (11):

$$n = \sqrt{\frac{|\varepsilon_c| + \varepsilon_{real}}{2}} \tag{10}$$

$$k = \sqrt{\frac{|\varepsilon_c| - \varepsilon_{real}}{2}} \tag{11}$$

where, $|\varepsilon_c| = \sqrt{\varepsilon_{real}^2 + \varepsilon_{imag}^2}$ is the complex modulus of permittivity.

By evaluating the attenuation corresponding to the two chemical potential situations, we are able to achieve ~1 dBμm^{-1} and ~0.08 dBμm^{-1}, respectively for $\mu_c = 0\ eV$ and $\mu_c = 1.325\ eV$.

Furthermore, and to properly evaluate the whole MMI structure and its behaviour when subjected to EM field radiation, we had to configure our simulation tools (BeamPROP [20], FemSIM [21] and FullWAVE [22]) accordingly. One must remember that the MMI device is too long to be simulated by the Finite Differences Time Domain (FDTD) method and that the Beam Propagation method is not accurate enough to simulate a graphene layer 0.7 nm high. Certainly, FullWAVE [22] is capable of performing a simulation over the entire 3D structure and, simultaneously, being able to "see" the 0.7 nm high graphene layer, only not within sensible limits of time.

Hence, our simulation domain had to be divided in three sections. Each section was handled by the appropriate software tool and the outcome results were passed over to the next simulation stage tool. The tool sequence followed were:

- Mode solver to determine the input field profile (FemSIM or ModeSolver);
- BeamPROP takes the outcome of previous tool and simulates its propagation until graphene section (54.7 μm);
- FullWAVE uses previous tool (BeamPROP) outcome results and simulates their propagation until the end of graphene section (55.7 μm);
- The output results of FullWAVE are passed on to BeamPROP which performs the simulation until the end of the device (110.4 μm).

Figure 7 and Figure 8 show the results obtained by FullWAVE, at the end of the graphene section and for both values of chemical potential. One is able to notice the amplitude difference verified between the two electric fields profiles, namely near the x-axis edges of the simulation domain. These results were obtained by applying simultaneously at the two graphene layers, the same chemical potential (either 0 eV or 1.325 eV).

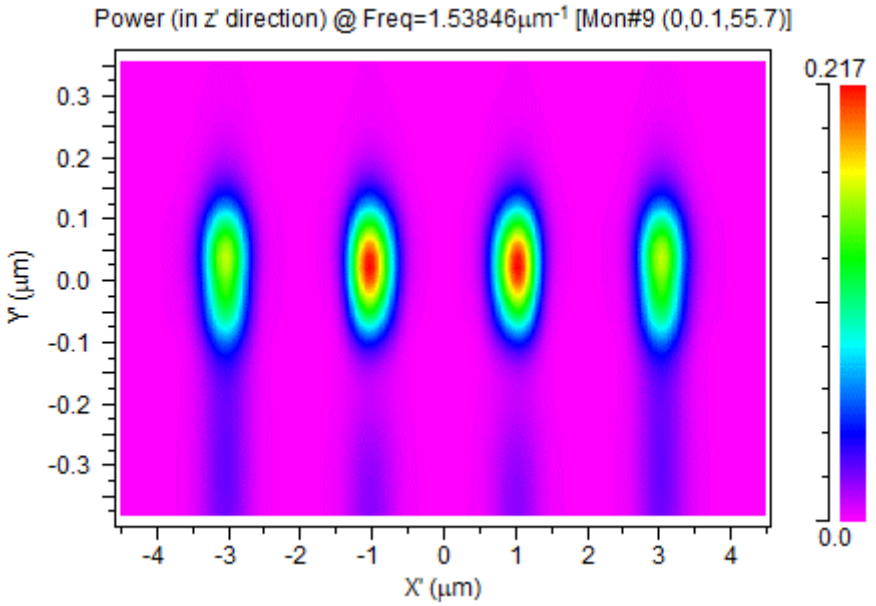

Figure 7 – E_X field profile at the end of graphene section when U_C = 0 eV.

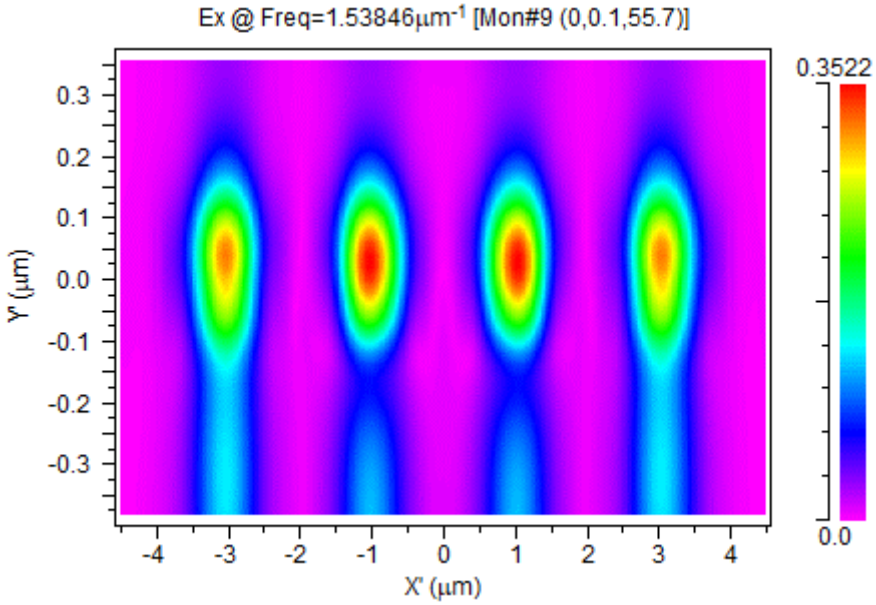

Figure 8 - E_X field profile at the end of graphene section when U_C = 1.325 eV.

4. CONCLUSIONS

Lithographic resolution presents a serious constraint on MMI devices performance. In this work and through simulation, we have presented and proposed two different strategies to mitigate the impact of limited lithographic mask resolution. The approach where tapered access waveguides were simulated, has revealed that the power imbalance between the output waveguides and insertion loss can be both minimized by using linear tapers with specific width. This work is in accordance with analytical predictions calculated by Hill et al. [11] and where it is stated that there is an optimal ratio between the multimode section and the tapers widths.

In our second approach, we propose a dynamic control of the optical conductivity of graphene through electrical gating. By adjusting the EM field amplitude in precise locations within the multimode section, we should be able to minimize the power imbalance at the output waveguides. This could be achieved through a negative/positive feedback system that monitors the power at each output waveguide and controls the gating bias that is applied to graphene. Our simulations showed that, by biasing graphene, the attenuation of the EM field amplitude can have a variation of almost two orders of magnitude, which offers good prospects for power imbalance reduction.

Further work will consist on evaluating the impact of graphene gating on the phase of the EM field and possible applications, and also on optimizing the multilayer structure by conducting simulations with different semiconductors.

Acknowledgements: This research has been supported by EU funds through the FEDER European Regional Development Fund and by Portuguese national funds provided by FCT – Fundação para a Ciência e a Tecnologia through grant SFRH/BD/144833/2019 and projects PTDC/NAN-OPT/31311/2017 and UID/EEA/00066/2019, and by projects IPL/2019/BioPlas_ISEL and IPL/2019/MO-TFT_ISEL.

REFERENCES

[1] L. R. Harriott, "Limits of lithography," *Proc. IEEE*, vol. 89, no. 3, pp. 366–374, 2001.
[2] M. Watanabe, "Active Matrix Driving and Circuit Simulation," *Featur. Liq. Cryst. Disp. Mater. Process.*, 2011.
[3] N. Yamauchi, Y. Inaba, and M. Okamura, "An integrated photodetector-amplifier using a-Si p-i-n photodiodes and poly-Si thin-film transistors," *IEEE Photonics Technol. Lett.*, vol. 5, no. 3, pp. 319–321, Mar. 1993.
[4] R. Takei, "Amorphous Silicon Photonics," in *Crystalline and Non-crystalline Solids*, InTechOpen, 2016, p. 21.
[5] S. K. Selvaraja *et al.*, "Low-loss amorphous silicon-on-insulator technology for photonic integrated circuitry," *Opt. Commun.*, vol. 282, no. 9, pp. 1767–1770, 2009.
[6] "Refractive index database." [Online]. Available: https://refractiveindex.info/. [Accessed: 02-Mar-2020].
[7] P. Lourenço, A. Fantoni, and M. Vieira, "Simulation analysis of a thin film semiconductor MMI 3dB splitter operating in the visible range," in *Fourth International Conference on Applications of Optics and Photonics*, 2019, p. 4.
[8] P. Lourenço, A. Fantoni, J. Costa, and M. Vieira, "Lithographic mask defects analysis on an MMI 3 dB splitter," *Photonics*, vol. 6, no. 4, pp. 1–8, 2019.
[9] L. B. Soldano and E. C. M. Pennings, "Optical Multi-Mode Interference Devices Based on Self-Imaging : Principles and Applications," *J. Light. Technol.*, vol. 13, no. 4, pp. 615–627, 1995.
[10] G. Lifante, *Integrated Photonics: Fundamentals*. Chichester, UK: John Wiley & Sons, Ltd, 2003.
[11] M. T. Hill, X. J. M. Leijtens, G. D. Khoe, and M. K. Smit, "Optimizing imbalance and loss in 2 × 2 3dB multimode interference couplers via access waveguide width," *OSA Trends Opt. Photonics Ser.*, vol. 88, no. 10, pp. 1343–1345, 2003.
[12] A. A. Balandin *et al.*, "Superior thermal conductivity of single-layer graphene," *Nano Lett.*, vol. 8, no. 3, pp. 902–907, 2008.
[13] F. Bonaccorso, Z. Sun, T. Hasan, and A. C. Ferrari, "Graphene photonics and optoelectronics," *Nat. Photonics*, vol. 4, no. 9, pp. 611–622, 2010.
[14] F. Wang *et al.*, "Gate-variable optical transitions in graphene," *Science (80-.).*, vol. 320, no. 5873, pp. 206–209, 2008.
[15] Z. Lu and W. Zhao, "Nanoscale electro-optic modulators based on graphene-slot waveguides," *J. Opt. Soc. Am. B*, vol. 29, no. 6, p. 1490, Jun. 2012.
[16] M. Silveirinha and N. Engheta, "Tunneling of electromagnetic energy through subwavelength channels and bends using ε-near-zero materials," *Phys. Rev. Lett.*, vol. 97, no. 15, 2006.
[17] R. Liu *et al.*, "Experimental demonstration of electromagnetic tunneling through an epsilon-near-zero metamaterial at microwave frequencies," *Phys. Rev. Lett.*, vol. 100, no. 2, pp. 1–4, 2008.
[18] R. Sun *et al.*, "Transparent amorphous silicon channel waveguides with silicon nitride intercladding layer," *Appl. Phys. Lett.*, vol. 94, no. 14, 2009.
[19] "Synopsys RSoft Solutions." [Online]. Available: https://www.synopsys.com/optical-solutions/rsoft.html. [Accessed: 02-Nov-2019].

[20] “BeamPROP.” [Online]. Available: https://www.synopsys.com/photonic-solutions/rsoft-photonic-device-tools/passive-device-beamprop.html. [Accessed: 04-Mar-2020].
[21] “FemSIM.” [Online]. Available: https://www.synopsys.com/photonic-solutions/rsoft-photonic-device-tools/passive-device-femsim.html. [Accessed: 04-Mar-2020].
[22] “FullWAVE - FDTD method.” [Online]. Available: https://www.synopsys.com/photonic-solutions/rsoft-photonic-device-tools/passive-device-fullwave.html. [Accessed: 29-Dec-2019].